RESEARCH ARTICLE

NANO · MICRO small
www.small-journal.com

Size-Dependent Penetration of Nanoparticles in Tumor Spheroids: A Multidimensional and Quantitative Study of Transcellular and Paracellular Pathways

Wenjing Chen, Wenqian Wang, Zhouzun Xie, Franco Centurion, Bin Sun, David J. Paterson, Simon Chang-Hao Tsao, Dewei Chu, Yansong Shen, Guangzhao Mao, and Zi Gu**

Tumor penetration of nanoparticles is crucial in nanomedicine, but the mechanisms of tumor penetration are poorly understood. This work presents a multidimensional, quantitative approach to investigate the tissue penetration behavior of nanoparticles, with focuses on the particle size effect on penetration pathways, in an MDA-MB-231 tumor spheroid model using a combination of spectrometry, microscopy, and synchrotron beamline techniques. Quasi-spherical gold nanoparticles of different sizes are synthesized and incubated with 2D and 3D MDA-MB-231 cells and spheroids with or without an energy-dependent cell uptake inhibitor. The distribution and penetration pathways of nanoparticles in spheroids are visualized and quantified by inductively coupled plasma mass spectrometry, two-photon microscopy, and synchrotron X-ray fluorescence microscopy. The results reveal that 15 nm nanoparticles penetrate spheroids mainly through an energy-independent transcellular pathway, while 60 nm nanoparticles penetrate primarily through an energy-dependent transcellular pathway. Meanwhile, 22 nm nanoparticles penetrate through both transcellular and paracellular pathways and they demonstrate the greatest penetration ability in comparison to other two sizes. The multidimensional analytical methodology developed through this work offers a generalizable approach to quantitatively study the tissue penetration of nanoparticles, and the results provide important insights into the designs of nanoparticles with high accumulation at a target site.

1. Introduction

Nanoparticles have been developed to offer new strategies for disease diagnosis and treatment owing to their unique advantages in drug delivery, gene therapy, bio-imaging, and many other biomedical applications.[1–3] For example, engineered liposomes, protein, and polymeric nanoparticles have been used to deliver small molecule drugs for cancer therapy,[4] and many formulations have been approved by the US Food and Drug Administration (FDA), such as doxorubicin-loaded liposome (DOXIL), albumin-bound paclitaxel (Abraxane), and paclitaxel-incorporated polymeric micelle (Genexol PM).[5–7] Gold nanoparticles (AuNPs) and iron oxide nanoparticles, among the FDA approved inorganic nanoparticles, have shown great promises in photothermal therapy and magnetic resonance imaging diagnosis.[8,9] Despite these advances, the development of nanoparticles for preclinical and clinical uses has encountered many challenges and faces high failure rate in clinical trials.[10] One of the primary reasons is the presence of biological barriers and dense

W. Chen, W. Wang, Z. Xie, F. Centurion, B. Sun, Y. Shen, G. Mao, Z. Gu
School of Chemical Engineering
University of New South Wales
Sydney, NSW 2052, Australia
E-mail: guangzhao.mao@unsw.edu.au; zi.gu1@unsw.edu.au

The ORCID identification number(s) for the author(s) of this article can be found under https://doi.org/10.1002/smll.202304693

DOI: 10.1002/smll.202304693

W. Chen, F. Centurion, Z. Gu
Australian Centre for NanoMedicine
University of New South Wales
Sydney, NSW 2052, Australia

D. J. Paterson
Australian Synchrotron ANSTO
Clayton, VIC 3168, Australia

S. C.-H. Tsao
School of Natural Sciences
Macquarie University
Sydney, NSW 2109, Australia

extracellular matrix (ECM) hindering the transport of nanoparticles in biological systems and their tissue penetration.[11,12]

To improve the penetration of nanoparticles into tumor tissues, it is crucial to gain a better understanding of the influencing factors and penetration pathways. The physicochemical properties of nanoparticles such as particle size, shape, and surface charge have been identified as important factors influencing tissue penetration.[13–15] For example, the penetration of different sizes of fluorescently labeled polystyrene nanoparticles in cell spheroids was investigated using confocal microscopy and fluorescence-activated cell sorting.[16–18] However, the existing studies are limited in using fluorescent dye labeled nanoparticles, which are associated with the issues of leaching and bleaching of fluorescent dyes.[19] Previous studies have identified two tissue penetration pathways of nanoparticles, which are transcellular and paracellular pathways.[20,21] The transcellular pathway is the transport of nanoparticles in tissues by crossing the cell membrane and interior of a cell.[22,23] The transcellular pathway includes energy-dependent (active) and energy-independent (passive) pathway, which requires and does not require the use of energy generated by adenosine triphosphate, respectively.[24] Paracellular transport involves the movement of particles through the extracellular matrix in the spaces between cells, which is energy-independent and follows a downhill gradient.[22] Nevertheless, quantitative studies on the pathways of tissue penetration and the associated particle size effect remain underexplored.

Herein, we developed a label-free, quantitative analytical method by integrating inductively coupled plasma mass spectrometry (ICP-MS), two-photon microscopy, and synchrotron X-ray fluorescence microscopy (XFM) to study the distribution and penetration pathways of AuNPs of different sizes in a tumor cell spheroid model (**Figure 1**). While several techniques have been employed to investigate the penetration of gold nanoparticles,[14,25–27] the key distinction of the three techniques that we selected to use lies in their direct quantification of AuNPs in cells and in spheroids, eliminating the need for additional compounds to modify AuNPs. To study the tissue penetration pathways, a classic inhibitor sodium azide (NaN_3) was used to block the energy-dependent transcellular pathway, which was compared with the groups without sodium azide treatment. By combining the findings through inductively coupled plasma mass spectrometry, two-photon microscopy, and synchrotron X-ray microscopy in 2D and 3D tumor models, we identified a correlation between nanoparticle size and penetration pathways, which provides insights for the future design of nanomedicines for promoting the tissue penetration of nanosystems and efficient treatment and diagnosis of diseases.

S. C.-H. Tsao
Department of Surgery
Austin Hospital
University of Melbourne
Melbourne, VIC 3084, Australia
D. Chu
School of Materials Science and Engineering
University of New South Wales
Sydney, NSW 2052, Australia
Z. Gu
UNSW RNA Institute
University of New South Wales
Sydney, NSW 2052, Australia

2. Results and Discussion

2.1. Synthesis and Characterization of AuNPs

Citrate-protected AuNPs of different sizes (15, 22, and 60 nm) were synthesized to study the effect of particle size on tissue penetration behavior in tumor spheroids. Under transmission electron microscope (TEM), the AuNPs appeared to be quasi-spherical in shape, and the average particle size was measured to be 15, 22 and 60 nm and was denoted AuNP-15, AuNP-22, and AuNP-60, respectively (**Figure 2**a–c). Dynamic light scattering (DLS) measurement showed the average hydrodynamic sizes of AuNP-15, AuNP-22, and AuNP-60 to be 17, 35, and 67 nm (Figure 2d). The zeta potential of all AuNPs was ≈−35 mV, without significant differences amongst different sizes (Figure 2e). The formation of AuNPs was characterized by UV–vis absorption spectroscopy, where the maximum absorbance peaks ≈520 nm were ascribed to the surface plasma resonance of AuNPs (Figure 2f). When the particle size increased from 15 to 60 nm, the maximum absorbance peak exhibited a red-shift, which is consistent with the previous study.[28] The crystallinity of the synthesized AuNPs with different sizes was investigated by X-ray diffraction (XRD). As shown in Figure 2g, the XRD patterns exhibited four distinct peaks, which corresponded to standard Bragg reflections (111), (200), (220), and (311) of a face-centered cubic lattice, confirming the crystalline nature of the AuNPs. This pattern is consistent with previous reports of the AuNPs nanocrystals.[29] As the particle size decreased from 60 to 15 nm, a broadening of the peaks was observed, which is attributed to the Scherrer equation. The broadening observed in smaller particles is due to incomplete constructive interference, meaning that there are an insufficient number of Bragg planes to accurately determine the diffraction angle.[30]

2.2. Size-Dependent Cellular Uptake Pathway in 2D Monolayer Cell Culture

Nanoparticles are known to be internalized into cells via various pathways, with specific uptake mechanisms dependent on factors such as nanoparticle size, shape, and surface charge. To elucidate the mechanism of cellular internalization of the AuNPs with different sizes, NaN_3, a typical inhibitor to block energy-dependent cellular uptake pathways was used to treat MDA-MB-231 cells.[31–33] The MDA-MB-231 was selected to use as a model cancer cell line because 1) the MDA-MB-231 is epithelial, and can form well-defined tumor spheroids with growth and proliferation characteristics,[34] and 2) using the MDA-MB-231 as a model to study the mechanism of nanomedicine improves fundamental understanding of nanomedicine approach to treat triple-negative breast cancer.[35]

The potential cytotoxicity of AuNPs and NaN_3 was first assessed in MDA-MB-231 cell cultures by using CCK-8 assay and Calcein-AM staining. The value of cell viability in each treatment group was normalized by comparing it with the control

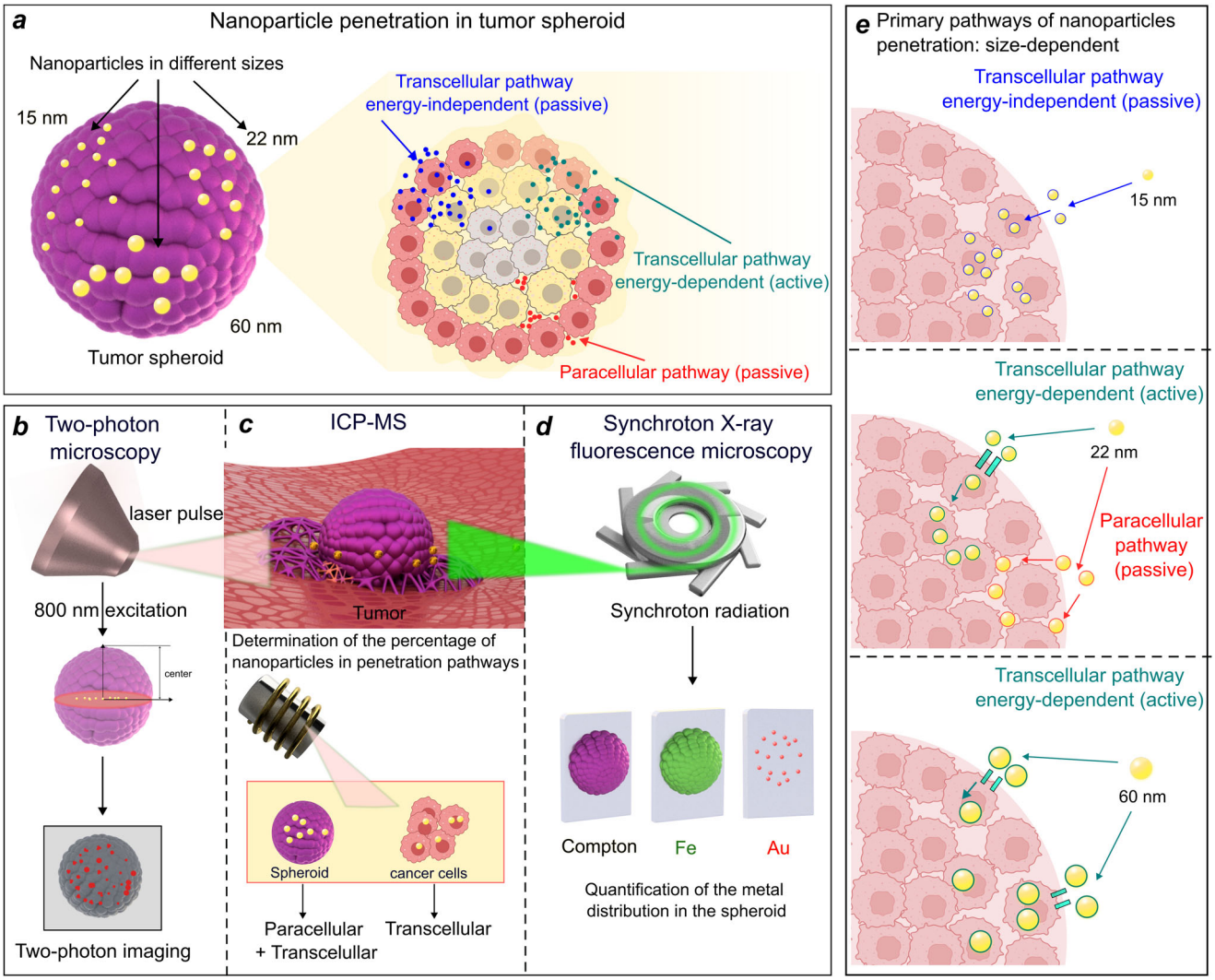

Figure 1. Schematic illustration of the size-dependent nanoparticle tissue penetration pathway study by using multi-dimensional, quantitative analytical methods.

group. As shown in Figure S1, Supporting Information, when the cells were incubated with 1 μg mL^{-1} AuNPs (the concentration used in the following experiments) for 24 h, the cell viability was 97% with no significant difference with the control. Hence, the AuNPs at 1 μg mL^{-1} were tolerable to the MDA-MB-231 cells. When the cells were treated with 0.65 mg mL^{-1} NaN_3 for different time intervals, the cell viability remained at ≈80% up to 16 h, showing no significant impact on cell growth (Figure S2, Supporting Information). The intracellular trafficking of AuNPs was conducted via CellLight Lysosome-GFP labeling to examine the colocalization of AuNPs with lysosomes. The colocalization analysis was conducted using Li's Intensity Correlation Quotient (ICQ) method,[36] which showed 0.415 and 0.406 for 2D and 3D respectively (Figure S3, Supporting Information), indicating the cellular uptake of AuNPs underwent endocytosis pathway.

Next, the cellular uptake of AuNPs in MDA-MB-231 breast cancer cells with or without NaN_3 treatment was examined by two-photon microscopy. In the representative two-photon microscopy images of cells (**Figure 3**), the red fluorescence signal corresponded to the two-photon excited luminescence signal from AuNPs. Mean fluorescence intensity (MFI) in the AuNP treated cells without NaN_3 treatment was used as a control to normalize the fluorescence signal intensity (Figure 3c,f,i). The results clearly showed that the addition of NaN_3 resulted in a significant decrease in the uptake of AuNP-22 and AuNP-60, whereas there were almost no significant differences between the uptake of AuNP-15 between the cells treated with and without NaN_3. It is likely due to the different cellular uptake mechanisms of nanoparticles with different sizes. After using NaN_3 to inhibit the energy-dependent cellular uptake, AuNP-15 entered cells through energy-independent cellular uptake, whereas no significant cellular internalization of AuNP-22 and AuNP-60 was observed, suggesting that AuNP-15 are likely to enter cells mainly through the energy-independent (passive) pathway while the cellular uptake of AuNP-22 and AuNP-60 is primarily through the energy-dependent (active) pathway. Our findings are in line with the previous study which indicated that nanoparticles smaller

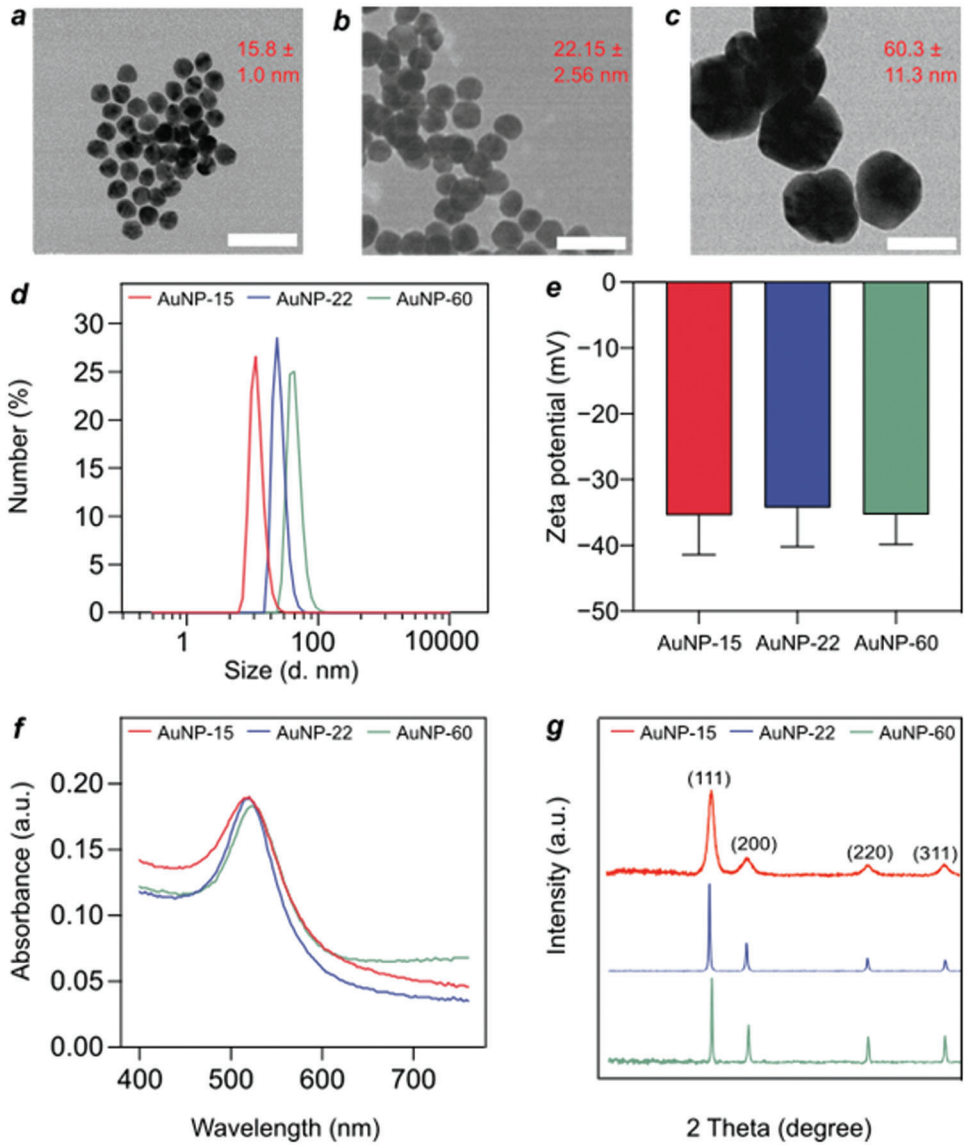

Figure 2. Physiochemical characterizations of 15, 22, and 60 nm gold nanoparticles (AuNP-15, AuNP-22, AuNP-60). a–c) Representative TEM images. Scale bar = 50 nm. d) Size measurements via DLS. e) Zeta potential measurement. f) UV–visible spectra. g) XRD patterns.

than 20 nm mostly exhibit an energy-independent cellular uptake.[37–39] In addition, the results, particularly the amount of internalized AuNPs reduced by 80% in cells treated with NaN_3 and AuNP-60, validated the feasibility of using NaN_3 to inhibit energy-dependent cellular uptake of AuNPs and prevent the active transport that requires energy in the transcellular pathways.

2.3. Effect of Particle Size on Tissue Penetration in Tumor Spheroids: an ICP-MS Study

To investigate the tissue penetration behavior of AuNPs of different sizes, MDA-MB-231 tumor spheroids have been developed (Figure S4, Supporting Information). Tumor spheroids have been shown as a superior model to mimic tumor tissue characteristics and provide an important experimental tool for understanding the localized spatiotemporal behaviors of nanoparticles.[40]

To examine how AuNPs penetrate in tumor spheroid and internalized by cells, the spheroids were incubated with different sizes of AuNPs. After 12 h incubation, the spheroids were either directly digested or dissociated into individual cells followed by washing and digestion for ICP-MS measurement. The ICP-MS results obtained from the direct digestion group indicate the total amount of AuNPs in the spheroids, while the results from the latter group suggest the amount of AuNPs delivered through the transcellular pathway. The total amount of AuNPs in spheroids follows the sequence: AuNP-22 > AuNP-15 > AuNP-60 (**Figure 4**a). The tissue penetration ability of AuNP-60 in the spheroids was

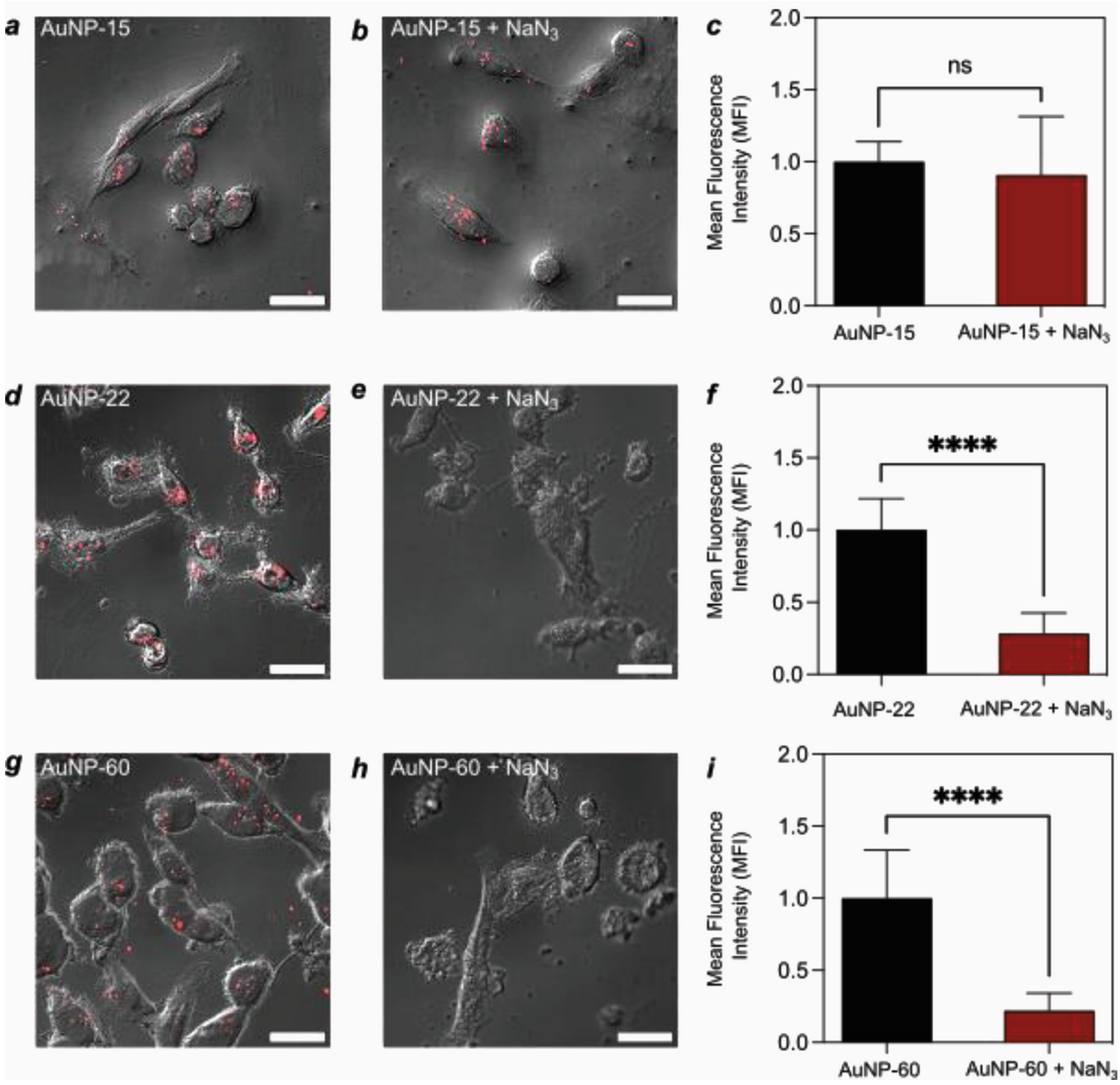

Figure 3. Two-photon microscopy analysis of cellular uptake of AuNP-15, AuNP-22, and AuNP-60 in MDA-MB-231 monolayer cells. a,d,g) Microscopy images of cells treated with AuNPs were obtained by merging bright field images and two-photon microscopy images. b,e,h) Microscopy images of cells treated with AuNPs and NaN_3 were obtained by merging bright field images and two-photon microscopy images. c,f,i) Fluorescence intensity analysis of two-photon microscopy images. Scale bar = 25 µm. (ns: not significant, ****$p \leq 0.0001$).

significantly lower than that of AuNP-15 and AuNP-22. Although AuNP-22 showed slightly increased penetration than AuNP-15, there was no significant difference between AuNP-15 and AuNP-22.

Next, the ratio of transcellular and paracellular pathways was obtained by calculating the average amount of AuNP in different groups representing transcellular and transcellular + paracellular pathways (Figure 4b). In the spheroids treated with different sizes of AuNPs, the transcellular pathway appeared to be a dominant mechanism of nanoparticle penetration, accounting for 91%, 63%, and 75% of total penetration of AuNP-15, AuNP-22, and AuNP-60, respectively. Amongst the three different sizes of AuNPs, the percentage of paracellular transport of AuNP-22 was the highest, which is attributed to the highest amount of AuNPs entering the spheroids. On the other hand, the AuNP-15 showed the lowest ratio of penetrating through the space between cells, indicating a transcellular pathway-dependent pathway.

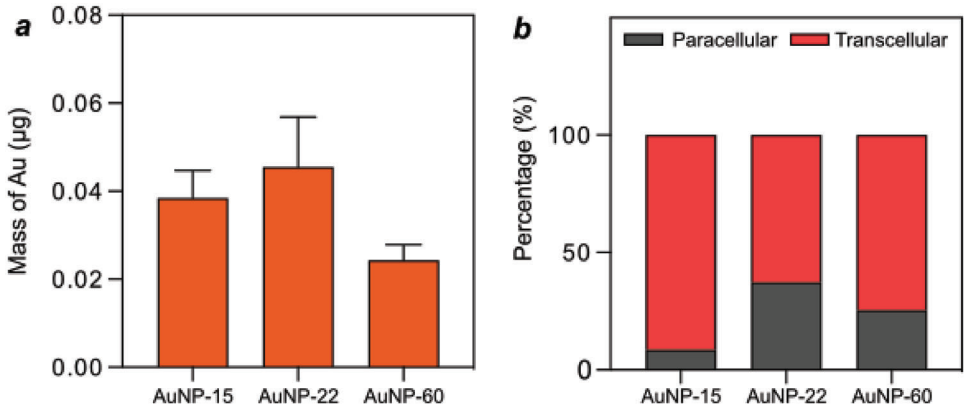

Figure 4. ICP-MS analysis of MDA-MB-231 spheroids treated with AuNPs. a) Mass of AuNPs with different sizes in tumor spheroids. b) The percentages of AuNPs that penetrate the tumor spheroids via transcellular and paracellular pathways.

2.4. Effect of Particle Size on Tissue Penetration in Tumor Spheroids: a Two-Photon Microscopy Study

To visualize and further study the tissue penetration of AuNPs and the particle size effect, tumor spheroids with or without NaN_3 treatment were incubated with different sizes of AuNPs, and quantitative analysis of the distribution of AuNPs at different distances in the spheroids was obtained by using two-photon microscopy. To obtain the quantitative information, ImageJ software was used to calculate the mean fluorescence intensity (MFI) at 10 μm intervals from the outer layer to the core of the spheroid. The MFI values were compared to assess the penetration behavior of AuNPs of the same size under different treatments (Figure S5, Supporting Information). To further improve the accuracy and reproducibility of data analysis, we developed a custom analysis platform. This platform uses bright-field images to determine the boundary of the cell spheroids and calculates each signal-bearing pixel in the R channel of the gold nanoparticle fluorescence images. The intensities of all pixels at the same distance were summed up and plotted as a histogram of intensity versus distance. Normalization of the intensity was achieved by using the peak value of intensity obtained from the spheroids treated with each size nanoparticle without NaN_3 treatment (**Figure 5**c,f,i).

By comparing the fluorescence intensity of AuNPs in the presence or absence of NaN_3 we evaluated the penetration behavior of AuNP-15, AuNP-22, and AuNP-60. Interestingly, in the case of AuNP-15, there was no significant difference in the fluorescence intensity at each depth level with or without NaN_3 treatment, indicating that the permeation of AuNP-15 was not affected when the energy-dependent penetration pathway was blocked. This is likely due to AuNP-15 penetrating tumor spheroids mainly through the passive pathway, which does not require energy consumption. In contrast, the larger nanoparticles, AuNP-22 and AuNP-60, showed remarkably shorter penetration distances in the presence of NaN_3. The results are in line with previous research suggesting that nanoparticles smaller than 50 nm penetrate tumor spheroids via the passive pathway more easily than the larger particles.[41] After the energy-dependent pathway was inhibited by NaN_3, there was a pronounced reduction in penetration in the AuNP-60 treated spheroids, and their penetration through the energy-independent pathway was very limited compared to AuNP-15 and AuNP-22, showing that AuNP-60 penetrated in spheroids mainly through active transcellular pathway. In the case of AuNP-22, although their penetration into the spheroids was significantly reduced after the energy-dependent pathway was inhibited, the nanoparticles or part of them could still penetrate spheroids through the energy-independent pathway. This result, in combination with the ICP-MS result, suggests that AuNP-22 entered spheroids primarily via the active transcellular pathway but also through the paracellular pathway.

2.5. Effect of Particle Size on Tissue Penetration and Penetration Pathway in Tumor Spheroids: a Synchrotron XFM Study

To provide the quantitative and multi-dimensional analysis of tissue penetration, synchrotron-based XFM was used to examine the distribution of AuNPs with different sizes in tumor spheroids. Analysis of cryo-sections using XFM is expected to yield a reliable elemental distribution map, as it bypasses the need for chemical fixation and physical sectioning. This is the first time that XFM was used to study the relationship between particle size and tissue penetration pathways. Quantification was performed using GeoPIXE software on XFM images of the tumor spheroids treated with AuNP-15, AuNP-22, and AuNP-60 with or without NaN_3 treatment (**Figure 6**).

Among the spheroids treated with nanoparticles of different sizes, AuNP-22 showed the highest concentration peak (924 ppm), while AuNP-60 had the lowest (187 ppm). The results were consistent with the ICP study. Additionally, the penetration depth corresponding to the concentration peak of AuNP-60 (at 15 μm) was lower than those of AuNP-15 (at 21 μm) and AuNP-22 (at 22 μm). The results suggest the size-dependent penetration ability of AuNPs: AuNP-22 > AuNP-15 > AuNP-60.

Upon the addition of NaN_3 to block the active transport pathway, AuNP-60 could barely penetrate the spheroids, in contrast to AuNP-15 and AuNP-22 which showed the concentration peaks at about 200 ppm. Comparing the peak height and area of the AuNP-15, AuNP-22, and AuNP-60 with or without NaN_3 treatment, there was no obvious change in AuNP-15 while much

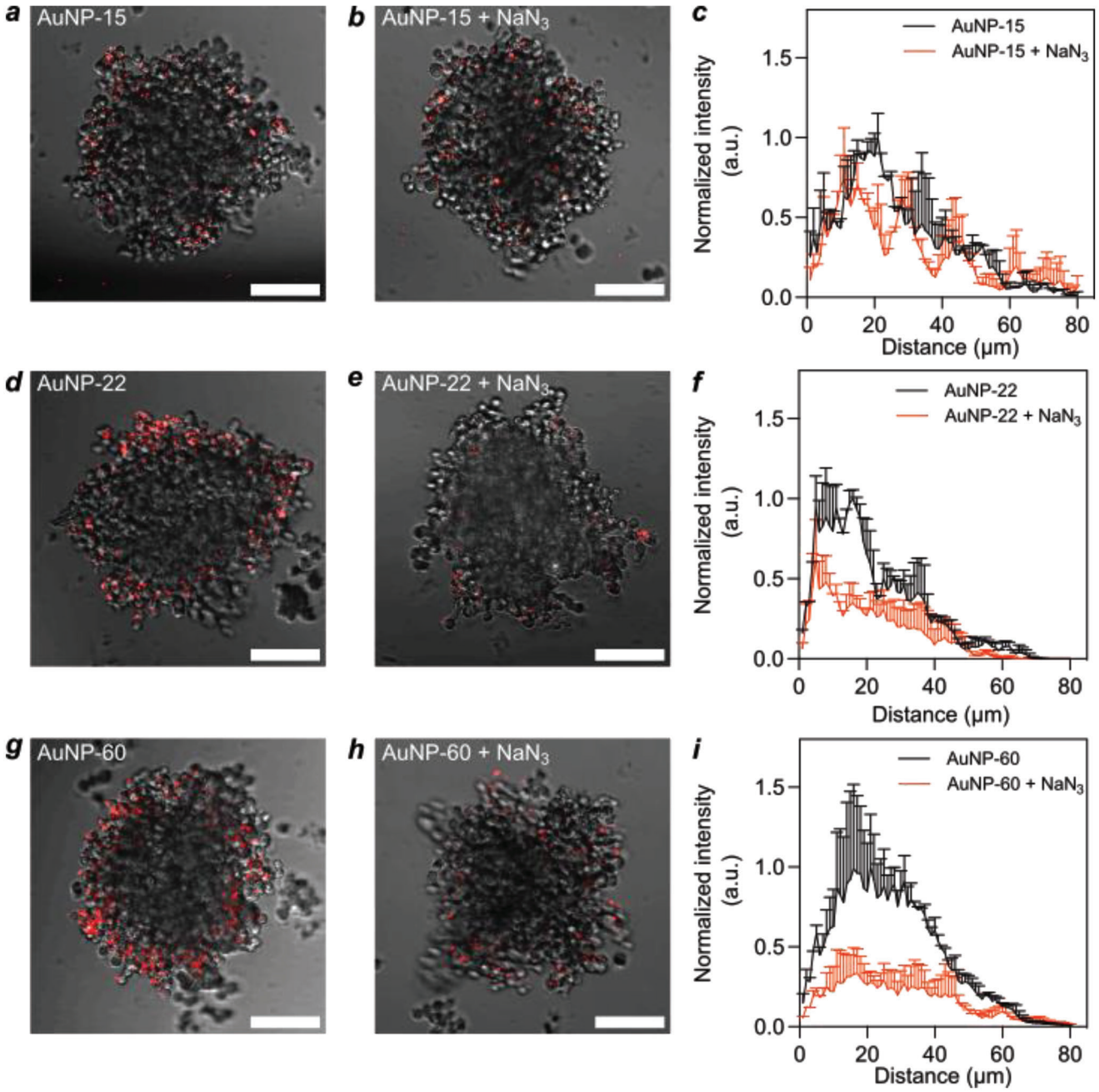

Figure 5. Two-photon microscopy analysis of tissue penetration of AuNP-15, AuNP-22, and AuNP-60 with or without NaN_3 in 3D MDA-MB-231 tumor spheroids. a,d,g) Microscopy images of spheroids treated with AuNPs were obtained by merging bright field images and two-photon microscopy images. b,e,h) Microscopy images treated with AuNPs and NaN_3 were obtained by merging bright field images and two-photon microscopy images. c,f,i) Fluorescence intensity analysis in different distances of two-photon microscopy images. Scale bar = 100 μm.

lower Au concentration in AuNP-22 and AuNP-60 after NaN_3 treatment. These findings were in accordance with the conclusions drawn from the two-photon results that suggested AuNP-15 predominantly penetrated tumor spheroids via passive transport pathway, whereas AuNP-60 primarily penetrated spheroids via active transcellular pathway. For AuNP-22, energy-dependent transport through the transcellular pathway was the primary mode of penetration, although some nanoparticles could permeate via the passive paracellular pathway, corresponding to the two-photon microscopy study.

From the above studies using various analytical methods, we observed that nanoparticles of different sizes penetrate tumor spheroids through distinct main pathways (Table S1, Supporting Information). AuNP-15, with its small size, can enter cells without energy requirement, likely due to its ability to cross the cell membrane without affecting membrane integrity. On the other

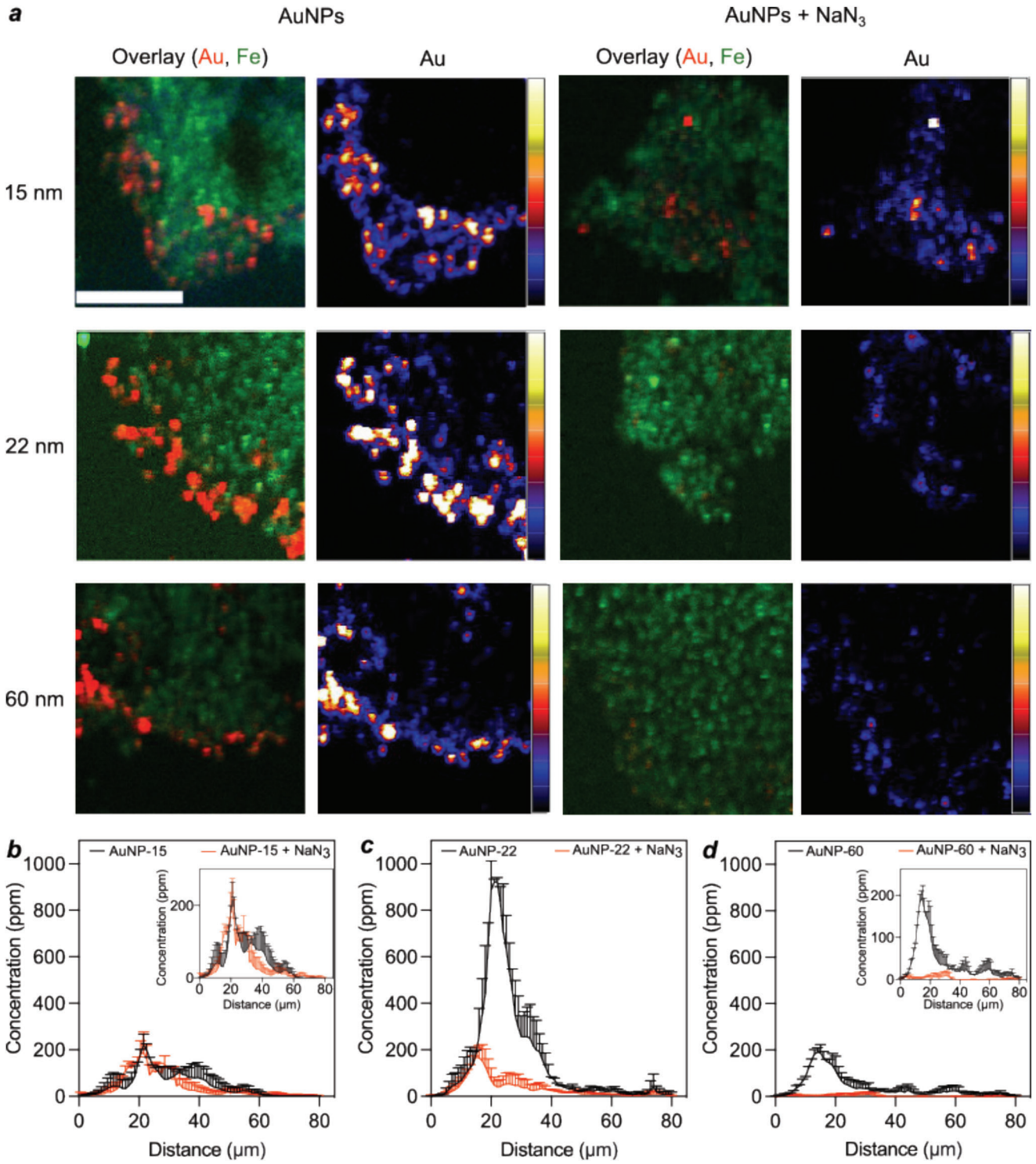

Figure 6. XFM analysis of tissue penetration of AuNP-15, AuNP-22, and AuNP-60 with or without NaN_3 in 3D MDA-MB-231 tumor spheroids. a) Elemental mapping of Au (representing AuNPs) and Fe (representing cells) in spheroids treated with AuNPs with or without NaN_3 and Au heat maps. Scale bar = 100 μm. b–d) Quantitative analysis of Au content in XFM images.

hand, the larger size of AuNP-60 hinders it from directly crossing the dense ECM and cell membrane, and its penetration relies on transcellular energy-dependent pathways for penetration. The size of AuNP-22 enables transport through the space between cells, but restricts the penetration pathway through directly crossing the membrane and energy is necessarily consumed for cellular uptake. Based on these findings, we conclude that the nanoparticles of 15 and 60 nm, whose main pathway is transcellular pathway, could be favorably applied in nanomedicine applications that require transport in the cell interior, such as gene therapy, while 22 nm nanoparticles, with its excellent penetration ability and both transcellular and paracellular pathway, can be used to deliver cargo to the central region of tumor tissues.

3. Conclusions

This work presented the particle size-dependent penetration behavior of nanoparticles in a tumor spheroid model by using a combination of analytical assays and techniques. AuNPs with same shape and surface charge but different particles sizes (15, 22, 60 nm) were synthesized, and used to treat MDA-MB-231 tumor cells and spheroids. The distribution and penetration pathways of AuNPs were visualized and quantified by using ICP-MS, two-photon microscopy, and synchrotron XFM. By combining the results from different analytical methods, it came to conclusions that the tissue penetration of 15 nm AuNPs was energy-independent (passive) transcellular pathway, while 60 nm AuNPs penetrated primarily through an energy-dependent (active) transcellular pathway. For the penetration of 22 nm AuNPs, although active transcellular pathway was dominant, both transcellular and paracellular pathways play an important role in determining the tissue distribution and demonstrated the greatest ability to penetrate tumor spheroids compared to the other two sizes. Overall, we have developed a multi-dimensional, quantitative analytical method to study tissue penetration of nanoparticles, which we believe can be used as a platform method to study penetration behavior of various nanoparticles in tissue samples. The findings through using this method provide insights to guide the design of other nanoparticle-based delivery systems.

4. Experimental Section

Materials: Gold (III) chloride trihydrate (≥ 99.9%, $HAuCl_4 \cdot 3H_2O$)), hydroquinone (99%), sodium azide (NaN_3), penicillin/streptomycin, Dulbecco's phosphate buffered saline (PBS), fluoromount aqueous mounting medium, poly-L-lysine, and hexamethyldisilazane (HMDS) were obtained from Sigma-Aldrich (Sydney, Australia). Tri-sodium citrate ($Na_2C_6H_5O_7{\cdot}2H_2O$) was bought from Ajax Finechem Pty Limited (Sydney, Australia). Nitric acid and hydrochloric acid were bought from RCI Labscan (Gillman, Australia). Dulbecco's modified eagle medium (DMEM, high glucose), Dulbecco's modified eagle medium: nutrient mixture F12 (DMEM/F12), B27 supplement, trypsin-EDTA (0.25%, phenol red), CellLight Lysosomes-GFP, BacMam 2.0, Dulbecco's phosphate buffered saline (PBS) were purchased from ThermoFisher (Sydney, Australia). Cell counting kit-8 (CCK-8) was bought from Abcam. Fetal bovine serum (FBS) was bought from Scientifix Pty Ltd (Clayton, Australia). Glutaraldehyde was bought from ProSciTech (Kirwan, Australia). Osmium tetroxide was bought from Electron Microscopy Sciences (Hatfield, USA). Ethanol was bought from ChemSupply (Gillman, Australia). Calcein-AM was purchased from Santa Cruz Biotechology (Dallas, USA) and Cryo-embedding compound was purchased from Ted Pella (Redding, USA). Milli-Q water and nitrogen gas were used from the own laboratory.

Synthesis of AuNPs: $HAuCl_4$ solution (0.1 mg mL^{-1}) was heated at 105 °C to a boil and mixed with 1.8 mL of trisodium citrate (10 mg mL^{-1}) with stirring at 500 rpm. After stirring for 10 min, it was cooled down to room temperature and then stirred for another 3 h to obtain 15 nm AuNPs, designated as AuNP-15.[42] To synthesize 22 nm AuNPs (AuNP-22), 14 mL of 15 nm AuNPs were added to a $HAuCl_4$ solution (90 mL of 0.11 mg mL^{-1}) with stirring at 750 rpm. The suspension was mixed with 0.22 mL of trisodium citrate (10 mg mL^{-1}), followed by the addition of 1 mL of hydroquinone (0.03 M). The following reaction was conducted for 3 h at room temperature while stirring at 750 rpm.[43,44] The 60 nm AuNPs (AuNP-60) were synthesized by following the same procedure of AuNP-22 synthesis but reducing the amount of 15 nm AuNPs from 14 to 3 mL.

Characterization of AuNPs: The morphology and size of the AuNPs were measured using a TEM (FEI Tecnaai G2). The particle size distribution and zeta potential analysis of AuNPs were conducted using Zetasizer Ultra (Malvern Panalytical). The absorption spectra of AuNP suspension were recorded on CLARIOstra Plate Reader. XRD measurements were performed using a PANalytical X-ray diffraction system with Co source at a scanning rate of 0.067° s^{-1} from 5° to 100°.

Cell Culture: MDA-MB-231, an epithelial human breast cancer cell line, was cultured in Dulbecco's modified eagle medium with 10%(v/v) fetal bovine serum, 1%(v/v) penicillin/streptomycin in a humidified atmosphere containing 5% CO_2 at 37 °C.

Tumor Spheroid Preparation: MDA-MB-231 spheroids were prepared by the liquid overlay method as previously described.[45] Briefly, cells were suspended at a density of 8×10^4 cells per mL in a mixture of DMEM/F12 medium containing B27 supplement (50×), 0.4% BSA, 1% penicillin/streptomycin, 20 ng mL^{-1} epidermal growth factor (EGF) and 5 μg mL^{-1} insulin. 200 μL of the cell suspension was seeded into each well of an ultra-low attachment 96-well plate (1600 cells per well). The culture medium was partially (100 μL) replaced with fresh medium every other day. At 5-day post cell seeding, the size of the cell spheroid reached about 250 μm in diameter.

Sample Preparation for Scanning Electron Microscopy Imaging: To observe spheroids' structure via scanning electron microscopy (SEM), 5-day-old spheroids (7000 cells/spheroid) were transferred to poly-L-lysine-coated coverslips. After incubating for 40 min at 37 °C, the spheroids were fixed overnight at 4 °C in 2.5% glutaraldehyde and stained with 1% osmium tetroxide using Pelco Biowave Pro+ Microwave processing system. Next, a serial ethanol dehydration protocol with 30%, 50%, 70%, 90%, and 100% was performed using the Biowave. The samples were then dried through a graduated series of ethanol:HMDS mixtures (2:1 ethanol:HMDS and 1:2 ethanol:HMDS, respectively) until pure HMDS. Finally, samples were glutted onto stubs, platinum-coated in Emitech K575x Pt sputter coater, and detected with InTouchScope SEM instrument (JSM).

Distribution Analysis of AuNPs in 2D and 3D Cell Cultures with Two-Photon Microscopy: For two-photon imaging analysis in 2D cell culture, MDA-MB-231 cells were seeded in a 24-well plate with coverslips at a density of 5×10^4 cells on one coverslip with a thickness of 0.17 mm. After 24 h incubation, the cells were treated with or without 0.65 mg mL^{-1} (10 mM) NaN_3. After 30 min treatment, the medium was then replaced with fresh medium containing 1 μg mL^{-1} 15, 22, and 60 nm AuNPs with or without 0.65 mg mL^{-1} (10 mM) NaN_3. After 12 h incubation, the cells were washed with PBS three times and fixed with 4% PFA. The coverslips were mounted on glass slides using aqueous mounting medium. Two-photon imaging was performed on a confocal laser scan microscope (Zeiss LSM 880) at 800 nm excitation wavelength to observe the distribution of AuNPs in the cells.[46] The images of cells in 2D and spheroids were acquired using a Plan-Apochromat 63x/1.4 Oil DIC M27 objective and a Plan-Apochromat 10x/0.45 M27 objective, respectively. To collect the two-photon photoluminescence (TPPL) emitted by the AuNPs, a band pass filter, FF01-641/75-25 (603.5–678.5 nm), was placed before a non-descanned detector on the microscope.

For two-photon imaging analysis in 3D spheroid cultures, the MDA-MB-231 spheroids were treated with or without 0.65 mg mL^{-1} NaN_3. After 30 min incubation, the medium was removed and replaced with fresh

medium containing 1 μg mL^{-1} AuNPs with or without 0.65 mg mL^{-1} NaN_3. After 12 h incubation, the spheroids were removed by pipet and gently washed with PBS and fixed with 4% PFA. The distribution of AuNPs in the spheroid was examined via two-photon imaging, using the same microscope settings as previously described.

Computational Image Segmentation Method for Analyzing Diffusion: A computational image segmentation method (CISM) was developed to assess AuNPs penetration in two-photon images of spheroids. This method had a higher resolution compared to conventional methods, capturing more detailed features. The images were pre-processed to 512 × 512 pixels and cropped them along the spheroid edge using Meta AI's tool.[47] The images were then imported to Python for edge detection and identification of "red points" – pixels with significantly more red than green or blue values. For each red point, the Euclidean distance to the nearest edge pixel was calculated and stored. This data, including point coordinates, the nearest edge, distance, and red intensity, was structured into a Pandas DataFrame and exported to a CSV file. Using this method, image information in one pixel resolution was extracted to calculate further measures such as AuNPs penetration distance and depth. The details of workflow and code logic have been provided in Figure S6, Supporting Information.

In Vitro Cellular Localization Studies of AuNPs: For cellular localization analysis in 2D cell culture, MDA-MB-231 cells were seeded on coverslips in a 24-well plate at a density of 5 × 10^4 cells. After 24 h incubation, the culture medium was replaced with media containing CellLight Lysosomes-GFP, BacMam 2.0 reagent by following the manufacturer's instructions, and was gently mixed. Then, the medium was replaced with fresh medium containing 1 μg mL^{-1} 22 nm AuNPs. After 12 h incubation, the cells were washed with PBS three times and fixed with 4% PFA. The coverslips were mounted on glass slides using aqueous mounting medium. For 3D spheroid analysis, the cells were cultured in the T25 flask, after the cells were well attached, the culture medium was replaced with medium containing CellLight reagent by following the manufacturer's instructions. After 16 h incubation, spheroids were produced as described in the method of tumor spheroid preparation and treated with AuNPs as described in the section. The cells and spheroids were observed under a confocal laser scan microscope (Zeiss LSM 880) with an excitation wavelength of 800 nm to observe the AuNPs at 505–545 nm excitation wavelength to observe the lysosomes. The colocalization was analyzed with Li's method using ImageJ JaCoP plugin.[36,48] Three individual cells and spheroids were randomly selected for the colocalization measurement.

ICP-MS Analysis of Tissue Penetration: The concentration of AuNPs in spheroids was quantitatively determined using ICP-MS. Spheroids were produced as described in the tumor spheroid preparation part and treated with AuNPs as described in the section on distribution analysis of AuNPs in 2D and 3D cell cultures with two-photon microscopy. At the end of treatment, 10 spheroids for each treatment group were collected using a pipette and washed with PBS. To measure the intracellular amount of AuNPs, spheroids were dissociated using trypsin-EDTA for 15 min, followed by washing with PBS. Spheroid samples were digested in aqua fortis composed of nitric acid and hydrochloric acid (3:1, v/v) before being subjected to ICP-MS.

Synchrotron XFM Analysis of Tissue Penetration: In an ultra-low attachment 96-well plate, 7000 cells were seeded per well and incubated for 5 days to generate spheroids of ≈300 μm in diameter. After washing with PBS and cryo-embedding, cryo-sectioning was performed using a microcryotome. Spheroids were sectioned in a thickness of 20 μm and mounted on silicon nitride windows for XFM analysis.[49] The samples were freeze-dried at −80 °C for 24 h and then stored in a dust-free container with desiccants at room temperature until analyzed.

The AuNPs distribution in the spheroid sections was quantitatively mapped using the X-ray fluorescence microscopy (XFM) beamline at the Australia Synchrotron.[50] A Kirkpatrick-Baez mirror microprobe was used in conjunction with a Maia 384 detector array, and excitation was with an 18.5 keV X-ray beam with the flux of 2 × 10^{10} photons per second focused to a 2 × 2 μm spot size. Dwell times ranged from 0.5 to 20 ms per pixel, depending on the samples and the concentration of the element of interest. XFM map spectra were fitted using GeoPIXE and pixel elemental concentrations were determined using a fundamental parameter approach with a model sample matrix of 20 μm thick cellulose.[51]

In Vitro Cell Viability Evaluation: MDA-MB-231 cells were seeded in a 96-well plate microplate at a density of 10^4 cells per well and allowed to adhere overnight. The culture medium was removed and replaced with a complete medium containing AuNPs at various concentrations (1, 5, 10, and 20 μg mL^{-1}). The cells without AuNP treatment were used as a control. After 24 h incubation, the cell viability was measured by using a CCK-8 cell viability kit. The absorbance was measured at 450 nm with a reference wavelength of 650 nm using a microplate reader.

The toxicity of NaN_3 treatment was assessed in MDA-MB-231 spheroid cultures using calcein-AM staining. Spheroids were treated with 0.65 mg mL^{-1} NaN_3 for 12, 16, and 24 h of incubation at 37 °C. After that, the medium was replaced with a fresh medium containing 4 μM calcian AM and incubated for 30 min. Fluorescence signals were recorded on an Olympus IX53 fluorescence microscope. ImageJ software was used to quantify the fluorescence intensity, and three images were analyzed for each time interval.

Statistical Analysis: The quantitative data were expressed as mean ± SD. Statistical differences were determined using the two-tailed Student's *t*-test to compare two groups through GraphPad Prism 9.0 (Graph Pad Software Inc.). Statistical significance was indicated as $*p \leq 0.05$, $**p \leq 0.01$, $***p \leq 0.001$, and $****p \leq 0.0001$.

Supporting Information

Supporting Information is available from the Wiley Online Library or from the author.

Acknowledgements

The authors acknowledge funding support from UNSW RNA Institute Seed Fund and NSW Cardiovascular Research Capacity Program. Part of this research was undertaken on the X-ray fluorescence microscopy (XFM) beamline at the Australian Synchrotron, part of ANSTO. The authors would like to thank Dr Daryl Howard and Dr Andrew Langendam at Australian Synchrotron ANSTO and Miss Lingqing Zong for their support in X-ray fluorescence microscopy imaging and analysis. The authors would like to acknowledge the facilities and the scientific and technical assistance provided by the Electron Microscope Unit and Microscopy Australia, Katharina Gaus Light Microscopy Facility at UNSW Sydney.

Open access publishing facilitated by University of New South Wales, as part of the Wiley - University of New South Wales agreement via the Council of Australian University Librarians.

Conflict of Interest

The authors declare no conflict of interest.

Data Availability Statement

The data that support the findings of this study are available from the corresponding author upon reasonable request.

Keywords

gold nanoparticles, paracellular pathway, tissue penetration, transcellular pathway, tumor spheroid

Received: June 4, 2023
Revised: September 16, 2023
Published online: October 11, 2023

[1] M. Kus-Liskiewicz, P. Fickers, I. B. Tahar, *Int. J. Mol. Sci.* **2021**, *22*, 10952.
[2] X. W. Zhang, F. Centurion, A. Misra, S. Patel, Z. Gu, *Adv. Drug Delivery Rev.* **2023**, *194*, 114709.
[3] Q. Y. Zhang, D. D. Zhou, G. C. Fang, H. X. Lu, J. F. Zeng, Z. Gu, *Adv. Mater. Interfaces* **2022**, *9*, 2101914.
[4] M. J. Mitchell, M. M. Billingsley, R. M. Haley, M. E. Wechsler, N. A. Peppas, R. Langer, *Nat. Rev. Drug Discovery* **2021**, *20*, 101.
[5] P. Ma, R. J. Mumper, *J. Nanomed. Nanotechnol.* **2013**, *4*, 1000164.
[6] W. J. Gradishar, *Expert Opin. Pharmacother.* **2006**, *7*, 1041.
[7] A. Rudra, R. M. Deepa, M. K. Ghosh, S. Ghosh, B. Mukherjee, *Int. J. Nanomed.* **2010**, *5*, 811.
[8] Z. R. Goddard, M. J. Marin, D. A. Russell, M. Searcey, *Chem. Soc. Rev.* **2020**, *49*, 8774.
[9] F. Soetaert, P. Korangath, D. Serantes, S. Fiering, R. Ivkov, *Adv. Drug Delivery Rev.* **2020**, *163*, 65.
[10] N. Desai, *AAPS J.* **2012**, *14*, 282.
[11] S. Barua, S. Mitragotri, *Nano Today* **2014**, *9*, 223.
[12] E. Blanco, H. Shen, M. Ferrari, *Nat. Biotechnol.* **2015**, *33*, 941.
[13] K. Y. Huang, H. L. Ma, J. Liu, S. D. Huo, A. Kumar, T. Wei, X. Zhang, S. B. Jin, Y. L. Gan, P. C. Wang, S. T. He, X. N. Zhang, X. J. Liang, *ACS Nano* **2012**, *6*, 4483.
[14] P. T. Sujai, M. M. Joseph, G. Saranya, J. B. Nair, V. P. Murali, K. K. Maiti, *Nanoscale* **2020**, *12*, 6971.
[15] J. C. Zhao, H. X. Lu, P. Xiao, M. H. Stenzel, *ACS Appl. Mater. Interfaces* **2016**, *8*, 16622.
[16] A. Tchoryk, V. Taresco, R. H. Argent, M. Ashford, P. R. Gellert, S. Stolnik, A. Grabowska, M. C. Garnett, *Bioconjugate Chem.* **2019**, *30*, 1371.
[17] I. Van Zundert, B. Fortuni, S. Rocha, *Nanomaterials* **2020**, *10*, 2236.
[18] V. Sokolova, J. F. Ebel, S. Kollenda, K. Klein, B. Kruse, C. Veltkamp, C. M. Lange, A. M. Westendorf, M. Epple, *Small* **2022**, *18*, 2201167.
[19] T. Thomsen, A. B. Ayoub, D. Psaltis, H. A. Klok, *Biomacromolecules* **2021**, *22*, 190.
[20] V. Sheth, L. Wang, R. Bhattacharya, P. Mukherjee, S. Wilhelm, *Adv. Funct. Mater.* **2021**, *31*, 2007363.
[21] D. T. Martin, J. M. Steinbach, J. C. Liu, S. Shimizu, H. Z. Kaimakliotis, M. A. Wheeler, A. B. Hittelman, W. M. Saltzman, R. M. Weiss, *Mol. Cancer Ther.* **2014**, *13*, 71.
[22] A. S. L. Yu, *Tissue Barriers* **2017**, *5*, 2509.
[23] H. X. Lu, R. H. Utama, U. Kitiyotsawat, K. Babiuch, Y. Jiang, M. H. Stenzel, *Biomater. Sci.* **2015**, *3*, 1085.
[24] A. Misra, *Challenges in Delivery of Therapeutic Genomics and Proteomics*, Elsevier, Amsterdam, Netherlands **2010**.
[25] M. M. Joseph, J. B. Nair, K. K. Maiti, T. S. Therakathinal, *Biomacromolecules* **2017**, *18*, 4041.
[26] H. X. Lu, J. Y. Su, R. Mamdooh, Y. M. Li, M. H. Stenzel, *Macromol. Biosci.* **2020**, *20*, 1900221.
[27] M. M. Joseph, A. N. Ramya, V. M. Vijayan, J. B. Nair, B. T. Bastian, R. K. Pillai, S. T. Therakathinal, K. K. Maiti, *Small* **2020**, *16*, 2003309.
[28] G. A. Lopez-Munoz, J. A. Pescador-Rojas, J. Ortega-Lopez, J. S. Salazar, J. A. Balderas-Lopez, *Nanoscale Res. Lett.* **2012**, *7*, 423.
[29] S. Krishnamurthy, A. Esterle, N. C. Sharma, S. V. Sahi, *Nanoscale Res. Lett.* **2014**, *9*, 627.
[30] G. S. Girolami, *X-ray Crystallography*, University Science Books: Mill Valley, CA, USA, **2016**.
[31] M. Durymanov, C. Kroll, A. Permyakova, J. Reineke, *Mol. Pharmaceutics* **2019**, *16*, 1074.
[32] G. Biddeci, G. Spinelli, M. Massaro, S. Riela, P. Bonaccorsi, A. Barattucci, F. Di Blasi, *Int. J. Nanomed.* **2021**, *16*, 4755.
[33] K. Kostarelos, L. Lacerda, G. Pastorin, W. Wu, S. Wieckowski, J. Luangsivilay, S. Godefroy, D. Pantarotto, J. P. Briand, S. Muller, M. Prato, A. Bianco, *Nat. Nanotechnol.* **2007**, *2*, 108.
[34] Z. Huang, P. Yu, J. Tang, *OncoTargets Ther.* **2020**, *13*, 5395.
[35] A. Amaro, G. Angelini, V. Mirisola, A. I. Esposito, D. Reverberi, S. Matis, M. Maffei, W. Giaretti, M. Viale, R. Gangemi, *OncoTargets Ther.* **2016**, *7*, 68803.
[36] Q. Li, A. Lau, T. J. Morris, L. Guo, C. B. Fordyce, E. F. Stanley, *J. Neurosci.* **2004**, *24*, 4070.
[37] H. Nakamura, S. Watano, *KONA Powder Part. J.* **2018**, *35*, 49.
[38] S. Behzadi, V. Serpooshan, W. Tao, M. A. Hamaly, M. Y. Alkawareek, E. C. Dreaden, D. Brown, A. M. Alkilany, O. C. Farokhzad, M. Mahmoudi, *Chem. Soc. Rev.* **2017**, *46*, 4218.
[39] P. Candeloro, L. Tirinato, N. Malara, A. Fregola, E. Casals, V. Puntes, G. Perozziello, F. Gentile, M. L. Coluccio, G. Das, C. Liberale, F. De Angelis, E. Di Fabrizio, *Analyst* **2011**, *136*, 4402.
[40] J. B. Kim, R. Stein, M. J. O'Hare, *Breast Cancer Res. Treat.* **2004**, *85*, 281.
[41] J. X. Ding, J. J. Chen, L. Q. Gao, Z. Y. Jiang, Y. Zhang, M. Q. Li, Q. C. Xiao, S. S. Lee, X. S. Chen, *Nano Today* **2019**, *29*, 100800.
[42] S. Huo, H. Ma, K. Huang, J. Liu, T. Wei, S. Jin, J. Zhang, S. He, X. J. Liang, *Cancer Res.* **2013**, *73*, 319.
[43] Y. C. Dong, M. Hajfathalian, P. S. N. Maidment, J. C. Hsu, P. C. Naha, S. Si-Mohamed, M. Breuilly, J. Kim, P. Chhour, P. Douek, H. I. Litt, D. P. Cormode, *Sci. Rep.* **2019**, *9*, 14912.
[44] D. Kumar, I. Mutreja, P. Sykes, *Nanotechnology* **2016**, *27*, 355601.
[45] Y. Yi, H. J. Kim, M. Zheng, P. Mi, M. Naito, B. S. Kim, H. S. Min, K. Hayashi, F. Perche, K. Toh, X. Y. Liu, Y. Mochida, H. Kinoh, H. Cabral, K. Miyata, K. Kataoka, *J. Controlled Release* **2019**, *295*, 268.
[46] T. D. Rane, A. M. Armani, *PLoS One* **2016**, *11*, e0167548.
[47] A. Kirillov, E. Mintun, N. Ravi, H. Mao, C. Rolland, L. Gustafson, T. Xiao, S. Whitehead, A. C. Berg, W.-Y. Lo, P. Dollár, R. Girshick, *Segment Anything* **2023**, arXiv:2304.02643, https://doi.org/10.48550/arXiv.2304.02643.
[48] R. J. Holmila, S. A. Vance, X. Chen, H. Wu, K. Shukla, M. S. Bharadwaj, J. Mims, Z. Wary, G. Marrs, R. Singh, A. J. Molina, L. B. Poole, S. B. King, C. M. Furdui, *Sci. Rep.* **2018**, *8*, 6635.
[49] T. Q. Liu, I. Kempson, M. de Jonge, D. L. Howard, B. Thierry, *Nanoscale* **2014**, *6*, 9774.
[50] D. L. Howard, M. D. de Jonge, N. Afshar, C. G. Ryan, R. Kirkham, J. Reinhardt, C. M. Kewish, J. McKinlay, A. Walsh, J. Divitcos, N. Basten, L. Adamson, T. Fiala, L. Sammut, D. J. Paterson, *J. Synchrotron. Radiat.* **2020**, *27*, 1447.
[51] C. G. Ryan, B. E. Etschmann, S. Vogt, J. Maser, C. L. Harland, E. van Achterbergh, D. Legnini, *Nucl. Instrum. Methods Phys. Res., Sect. B* **2005**, *231*, 183.